TRENDS IN SCIENCES 2026; 23(12): 13644
https://doi.org/10.48048/tis.2026.13644 RESEARCH ARTICLE

Ionospheric Response over Thailand to the 2022 Hunga Tonga-Hunga Ha'apai Eruption from GNSS and VHF Radar Observations

Paparin Jamlongkul[1,2], Suwicha Wannawichian[1,*], Larry J. Paxton[3], Clayton E. Cantrall[3], Pornchai Supnithi[4], Jirapoom Budtho[4], Napat Tongkasem[4], Thananphat Thanakulketsarat[5], Phimmasone Thammavongsy[4] and Michi Nishioka[6]

[1]*Department of Physics and Materials Science, Faculty of Science, Chiang Mai University, Chiang Mai 50200, Thailand*
[2]*National Astronomical Research Institute of Thailand (Public Organization), Chiang Mai 50180, Thailand*
[3]*Johns Hopkins University Applied Physics Laboratory, Laurel, Maryland 20723, United States*
[4]*School of Engineering, King Mongkut's Institute of Technology Ladkrabang, Bangkok 10520, Thailand*
[5]*KOSEN-KMITL, King Mongkut's Institute of Technology Ladkrabang, Bangkok 10520, Thailand*
[6]*National Institute of Information and Communications Technology (NICT), Tokyo 1838795, Japan*

([*]Corresponding author's e-mail: suwicha.w@cmu.ac.th)

Received: 19 February 2026, Revised: 8 June 2026, Accepted: 15 June 2026, Published: 20 July 2026

Abstract

This study reports ionospheric observations over Thailand during the period surrounding the Hunga Tonga-Hunga Ha'apai volcanic eruption on 15 January 2022 (~04:14 UT). These observations document substantial ionospheric variability over Thailand during a period influenced by volcanic forcing under concurrent geomagnetic activity, providing a regional reference for assessing potential impacts on radio propagation and communication systems. Total electron content (TEC) measurements from 4 GNSS receiver stations in Bangkok (KMI6), Chumphon (CPN1), and Nakhon Ratchasima (RUTI) in Thailand, and Vientiane (NUO2) in Laos were processed to derive vertical TEC (VTEC), detrended TEC (dTEC), and the rate-of-TEC index (ROTI). These parameters were examined using distance-time plots, time-stamped maps, and longitude stack graphs to characterize their temporal evolution, propagation features, and disturbance directions. A coherent disturbance signature was identified in both dTEC and ROTI approximately 8 h after the eruption, with dTEC perturbations reaching several tens of TECU and exceeding typical background variability for this region and period. The dTEC analysis reveals a large-amplitude feature near 12:00 UT with characteristics consistent with a traveling ionospheric disturbance (TID), propagating toward Thailand with an estimated horizontal propagation speed of ~312 ± 13 m/s. Concurrent ROTI enhancements appear at ~12:20 UT along the dTEC propagation path and persist for approximately 3 h. Equatorial plasma bubbles (EPBs) are identified using ROTI and corroborated by very high frequency (VHF) radar range-altitude-time intensity (RATI) observations from the CPN1 station. EPBs on 15 January showed larger horizontal and vertical extents (up to ~1,000 km and ~650 - 700 km, respectively) than those on 14 and 16 January. In addition to the main post-eruption interval, smaller perturbations in VTEC and dTEC are observed on 16 January, indicating possible contributions from other disturbance sources.

Keywords: Ionospheric response, Volcanic eruption, Hunga Tonga, Thailand, TEC, TID, EPB, GNSS, VHF radar

Introduction

The impact of the Hunga Tonga volcanic eruption (~04:14 UT on 15 January 2022) on the ionosphere has been widely investigated [1-11], particularly at global and regional scales. This study focuses on the ionospheric response over Thailand, a low-latitude region characterized by strong ionospheric variability,

and presents a detailed analysis of its temporal and spatial characteristics. The Hunga Tonga volcano is located at 20.54°S geographic latitude and 175.38°W geographic longitude in the South Pacific Ocean. Previous studies have shown that this eruption, hereafter referred to as the HT eruption, generated large-scale atmospheric and ionospheric disturbances that propagated over long distances and were detectable worldwide. During the HT eruption, an estimated 16 - 75 × 10^{15} J of thermal energy was released, generating a wide range of geophysical disturbances [3], including notable effects in the ionosphere. Consequently, significant Total electron content (TEC) perturbations were detected globally, even in regions thousands of kilometers away from the eruption source. These ionospheric disturbances are commonly analyzed through detrended TEC (dTEC) fluctuations, which reflect wave-like perturbations propagating outward from the eruption.

Numerous studies have reported traveling ionospheric disturbances (TIDs) associated with the Hunga Tonga eruption [2-11]. The HT eruption and its aftermath generated various atmospheric waves, including acoustic waves, gravity waves, and the Lamb wave [12]. Each wave type exhibits distinct propagation characteristics. In particular, the Lamb wave, a trapped surface mode with a nearly constant phase speed of approximately 300 m/s, propagated globally multiple times with minimal attenuation (e.g., [3,9]). Vadas *et al.* [13] analyzed Tonga-induced disturbances using observations from the High-resolution Thermospheric Imaging (MIGHTI) instrument onboard the Ionospheric Connection Explorer (ICON) satellite, reporting medium- to large-scale gravity waves with speeds ranging from 100 to 600 m/s. Heki [14] similarly reported ionospheric disturbances over Japan propagating at velocities comparable to atmospheric Lamb waves, suggesting efficient upward energy coupling from the troposphere into the ionosphere. These co-volcanic ionospheric disturbances often exhibit quasi-periodic TEC variations with periods of 12 - 30 min [15]. However, longer-period (> 1 h) gravity waves have also been emphasized in the thermosphere following the eruption [13], indicating that a broad spectrum of wave processes contributed to the observed ionospheric response.

TIDs may contribute to the formation of equatorial plasma bubbles (EPBs), in association with large-scale lower atmospheric disturbances, variations of the equatorial ionization anomaly (EIA), and magnetic field perturbations [3]. EPBs are ionospheric irregularities characterized by localized plasma density depletions, typically occurring at night in equatorial and low-latitude regions. They are primarily generated by the Rayleigh-Taylor instability (RTI), which develops when a denser plasma overlies a less dense one, allowing perturbations at the interface to grow and initiate EPB formation [16]. During their evolution, plasma depletion regions rise to higher altitudes due to polarization electric fields within the EPBs, resulting in structures that align along geomagnetic field lines and extend to low-latitudes away from the magnetic equator [17-19]. EPBs are most frequently observed shortly after the evening terminator, around 19:00 Local Time (LT). This enhanced occurrence is associated with the pre-reversal enhancement (PRE) of the zonal electric field, which drives upward ($\vec{E} \times \vec{B}$) drift of the F-region plasma, thereby steepening electron density gradients at the bottomside F-region [16]. In addition, EPBs can be influenced by additional mechanisms, including atmospheric gravity waves, medium-scale traveling ionospheric disturbances (MSTIDs), and thermospheric wind effects [20-22]. Global observations further show that increases in the rate of TEC index (ROTI) correspond to enhanced phase fluctuations and TEC variability, making it a useful indicator of EPB activity [23].

The plasma density irregularities associated with EPBs affect radio wave propagation and can disrupt a wide range of communication and navigation systems (e.g., [24]). One of the remote-sensing techniques used to study EPBs is the very high frequency (VHF) radar. Operating in the 30 - 300 MHz range, VHF radars transmit signals upward and receive backscattered echoes from ionospheric irregularities, such as EPBs [25]. Due to their wide spatial coverage and high temporal and spatial resolution, VHF radars enable detailed observations of EPB development [26]. Nighttime F-region field-aligned irregularities (FAIs) observed by VHF radar (e.g., 30.8 MHz) exhibit spatial patterns similar to EPBs, implying a close association [27]. In addition, mid-latitude FAIs have been reported

to occur in conjunction with MSTIDs [28]. One commonly used radar representation for investigating EPBs is the range-altitude-time intensity (RATI) plot, in which radar signal intensity (or power) is displayed as a function of time and altitude. This type of visualization provides information on the temporal evolution and vertical structure of ionospheric irregularities and is widely used to examine EPB development [26].

Thailand serves as a strategic observational region; however, despite extensive global and regional investigations of the HT eruption, detailed observational studies of ionospheric responses over Thailand using locally available Global Navigation Satellite System (GNSS) and radar instrumentation remain limited. Thailand is situated in the low-latitude ionosphere near the crest of the EIA, where strong electrodynamic processes and plasma instabilities generate significant spatial and temporal variability. Previous studies have shown that irregularities over Thailand typically occur at night, with spread F and pre-midnight scintillation often inhibited by geomagnetic activity [2,29]. Enhanced EPB activity has also been reported following the HT eruption, particularly over East and Southeast Asia [7,30], indicating that eruption-related disturbances may influence irregularity development in this region.

The combined use of GNSS and VHF radar observations provides complementary information on ionospheric processes. GNSS TEC measurements capture large-scale disturbances while VHF radar observations are sensitive to plasma irregularities associated with EPB development. While previous studies have primarily focused on large-scale disturbances derived from GNSS observations, this study integrates both datasets to enable concurrent analysis of wave propagation and irregularity development. This approach provides additional observational constraints on the possible coupling between atmospheric waves generated by the eruption and ionospheric instability processes in the low-latitude region.

In this study, we investigate the ionospheric response over Thailand, a region located far from the eruption source using GNSS and VHF radar observations. Because the eruption coincided with a geomagnetically disturbed interval, geomagnetic conditions must also be considered when interpreting the observed ionospheric disturbances. Therefore, geomagnetic indices are examined as external background diagnostics to contextualize the ionospheric observations and to compare the timing of the strongest ionospheric disturbances with the evolution of geomagnetic activity. Specifically, we (1) characterize TEC disturbances over Thailand during the HT eruption, (2) identify propagating wave signatures, and (3) examine irregularity-related activity such as EPBs under the influences of volcanic and geomagnetic conditions. The following sections describe the datasets and analysis methods used to examine these responses.

Data and methodology

GNSS-derived TEC observations over Thailand are analyzed to investigate ionospheric disturbances associated with the HT eruption. In this study, GNSS observations from the Global Positioning System (GPS), Galileo (GAL), and Quasi-Zenith Satellite System (QZS) were analyzed. Additional datasets, including radar measurements and geomagnetic indices, are used to identify wave-like structures, including TIDs, and ionospheric irregularities. The analysis enables characterization of disturbance features and their temporal and spatial evolution.

Data source

The representative grid positions closest to each GNSS receiver station are demonstrated by black crosses within the colored squares in **Figure 1**. These stations are located at CPN1 (10.76°N, 99.37°E) in Chumphon, Thailand (blue), KMI6 (13.77°N, 100.53°E) in Bangkok, Thailand (orange), RUTI (14.99°N, 102.12°E) in Nakhon Ratchasima, Thailand (red), and NUO2 (17.98°N, 102.63°E) in Vientiane, Laos (green) [31]. A summary of the ionospheric pierce point (IPP) ranges and median GLAT/GLON used for VTEC, dTEC, and ROTI analysis is provided in **Table 1**. In addition to TEC data, VHF radar data (transmitting at 39.65 MHz) were obtained from the Prachomklao VHF radar station (10.76°N, 99.37°E), located at the King Mongkut's Institute of Technology Ladkrabang (KMITL) Chumphon campus. These data were provided by the National Institute of Information and Communications Technology (NICT) and KMITL [26]. In geomagnetic coordinates, the Chumphon station is located at 1.33°N, 172.19°E. The radar operates with

5 beams at different azimuth angles: (Fd1) –48°, (Fd2) –24°, (Fd3) 0°, (Fd4) 24°, and (Fd5) 48°, spanning west to east, as seen in **Figure 2**. The RATI data measurements from the VHF radar (**Figure 2**) at the CPN1 station are included.

TEC and ROTI derivation

Slant total electron content (sTEC) is obtained from dual-frequency GNSS ranging observations and derived from dual-frequency carrier-phase measurements (L_1 and L_2). The geometry-free linear combination of carrier phase observables is employed to isolate the ionospheric contribution, which is proportional to sTEC [32,33]. The geometry-free carrier phase combination was first formed as:

$$L_I^j(t_k) = L_1 - L_2 = \lambda_1 \Phi_1^j(t_k) - \lambda_2 \Phi_2^j(t_k), \quad (1)$$

where $L_I^j(t_k)$ is the geometry-free carrier phase combination. $\Phi_1^j(t_k)$ and $\Phi_2^j(t_k)$ are the observed carrier phase of carrier phase ranges L_1 and L_2 in an epoch t_k of satellite pseudorandom noise (PRN), j. λ_1 and λ_2 are their wavelengths, corresponding to GNSS carrier frequencies f_1 and f_2 of 1,575.42 and 1,227.60 MHz, respectively. Accordingly, the sTEC can be calculated as [33]:

$$\mathrm{sTEC}^j(t_k) = \frac{1}{40.3} \frac{f_1^2 f_2^2}{f_1^2 - f_2^2} L_I^j(t_k) + C^j, \quad (2)$$

where 40.3 ($m^3\ s^{-2}$) is the ionospheric delay constant, relating TEC to the dispersive delay of GNSS signals. TEC is expressed in TEC unit (TECU), where 1 TECU = 10^{16} electrons m^{-2}. The term C^j, which includes the constant phase ambiguity and instrumental biases, is treated through a zero-level adjustment following the relative TEC approach of Pi *et al.* [23]. This procedure removes the constant offset in sTEC and allows the analysis to focus on short-term TEC fluctuations associated with ionospheric irregularities. The derived sTEC is then mapped to VTEC using a thin-shell ionospheric approximation [34,35]:

$$\mathrm{VTEC} = \mathrm{sTEC} \cos z', \quad (3)$$

where z' is the zenith angle at the ionospheric pierce point, defined as

$$z' = \arcsin\left(\frac{\mathrm{RE}\cos\alpha}{\mathrm{RE}+h}\right). \quad (4)$$

here, α is the satellite elevation angle, RE is the mean Earth radius, and h is the ionospheric shell height, assumed to be at 350 km, a commonly adopted value representing the F-region peak altitude. While this assumption may introduce small uncertainties in the absolute TEC values and spatial mapping, it does not significantly affect the relative variations, propagation characteristics, or main conclusions of the study. Compared to pseudorange-based TEC, carrier phase measurements provide significantly higher precision and are therefore more suitable for calculating ROT and ROTI, which are sensitive to small-scale TEC fluctuations [33]. To examine ionospheric irregularities, we use 1-s VTEC, 1-s dTEC, and 5-min ROTI parameters derived from 1-s sTEC observations recorded at 4 GNSS receiver stations: CPN1, KMI6, RUTI, and NUO2.

Detrended TEC (dTEC) was calculated by removing the slowly varying background component from the original sTEC time series. For each satellite arc, the background TEC was estimated using a centered 15-min moving average, and the detrended TEC was obtained as [36]:

$$\mathrm{dTEC}^j(t_k) = \mathrm{sTEC}^j(t_k) - \overline{\mathrm{sTEC}^j}(t_k), \quad (5)$$

where

$$\overline{\mathrm{sTEC}^j}(t_k) = \frac{1}{N} \sum_{m=k-N/2}^{k+N/2} \mathrm{sTEC}^j(t_m). \quad (6)$$

here, j denotes the satellite PRN, t_k is the observation epoch, and N is the number of samples within the 15-min smoothing window. With the 1-s sampling interval, $N = 900$, used in this study, the resulting dTEC represents short-period TEC fluctuations after removal of the slowly varying diurnal and large-scale ionospheric background.

The ROT describes the temporal variation of sTEC between consecutive epochs and is calculated as [23,37]

$$\mathrm{ROT}_k^j = \frac{\mathrm{sTEC}_k^j - \mathrm{sTEC}_{k-1}^j}{t_k - t_{k-1}}, \quad (7)$$

where j denotes the satellite observed within the receiver's field of view. k is the time of epoch, and $t_k - t_{k-1}$ is the sampling interval of 1 s. ROTI is then calculated as the standard deviation of ROT within a 5-min window:

$$ROTI = \sqrt{\langle ROT^2 \rangle - \langle ROT \rangle^2}. \quad (8)$$

High ROTI values indicate rapid TEC fluctuations and are commonly associated with ionospheric irregularities, including EPBs [30,36]. In this study, enhanced ROTI values reaching ~1 - 5 TECU/min were observed during 14 - 16 January (**Table 2**), indicating intensified small-scale plasma structuring during the disturbance interval. The 5-min window is appropriate for the 1-s GNSS sampling rate because it reduces random measurement noise while preserving short-timescale ionospheric variability associated with plasma irregularities and traveling disturbances. In addition, the 5-min interval is widely adopted in previous ROTI studies [23,37] and provides a balance between temporal resolution and statistical stability. This interval is therefore suitable for characterizing short-timescale ionospheric TEC fluctuations associated with TIDs and plasma irregularities.

Data analysis

The VTEC, dTEC, and ROTI data are analyzed using 3 complementary visualization formats: longitude stack graphs, distance-time plots, and time-stamped map plots. The longitude stack graphs in **Figures 3(a) - 3(c)** provide a clearer representation of amplitude variations in VTEC, dTEC, and ROTI, respectively, beyond what is apparent from the distance-time color scales. The distance-time plots in Figure 4 illustrate the propagation of wave-like ionospheric disturbances from the HT eruption toward Thailand and nearby regions calculated along the great-circle path from Hunga Tonga to the site, as well as their temporal evolution. For visualization purposes, the color scales for the 3 parameters are defined based on their respective minimum and maximum ranges. The VTEC scale uses the minimum and maximum values across all 3 days due to their similar ranges, whereas the dTEC and ROTI scales are determined from the minimum and maximum values observed before and after the eruption day, as summarized in **Table 2**. During key transition periods, the map plots in **Figures 5 - 7** show the spatial distribution of disturbances and their propagation directions. The data are ordered from bottom to top, corresponding to locations nearest to the HT eruption (with larger longitudes) at the bottom and progressively more distant locations (with smaller longitudes) toward the top.

Geomagnetic data

The geomagnetic activity was investigated using the SYM-H and Kp indices [38-39], shown in **Figure 3**. The SYM-H index is a 1-min-resolution measure of the globally symmetric disturbance magnetic field associated primarily with variations in the ring current. The minimum SYM-H value is commonly used to identify the main phase of a geomagnetic storm. The Kp index is a 3-h planetary geomagnetic activity index derived from standardized magnetometer observations at mid-latitude stations. Kp and SYM-H values were used to identify the timing and intensity of geomagnetic activity during the study period and to provide context for interpreting the observed ionospheric responses. These indices were not used as explanatory variables in a quantitative model but were examined as external diagnostics to contextualize the ionospheric observations under concurrent geomagnetic activity. The storm onset is identified at approximately 10:53 UT on 14 January, based on a local enhancement in the SYM-H index (~17 nT). The initial and main phases of the geomagnetic storm each lasted approximately 5 - 6 h. The end of the main phase is identified by the minimum SYM-H value, which occurred at around 22:30 UT on 14 January, when SYM-H reached approximately −100 nT and the Kp index reached 6−, indicating strong geomagnetic storm conditions. As shown in **Table 2**, geomagnetic indices were examined qualitatively alongside TEC-derived parameters to assess whether major ionospheric disturbances coincided with periods of strongest geomagnetic activity or occurred preferentially following the eruption. The associated ionospheric responses are discussed in the next section.

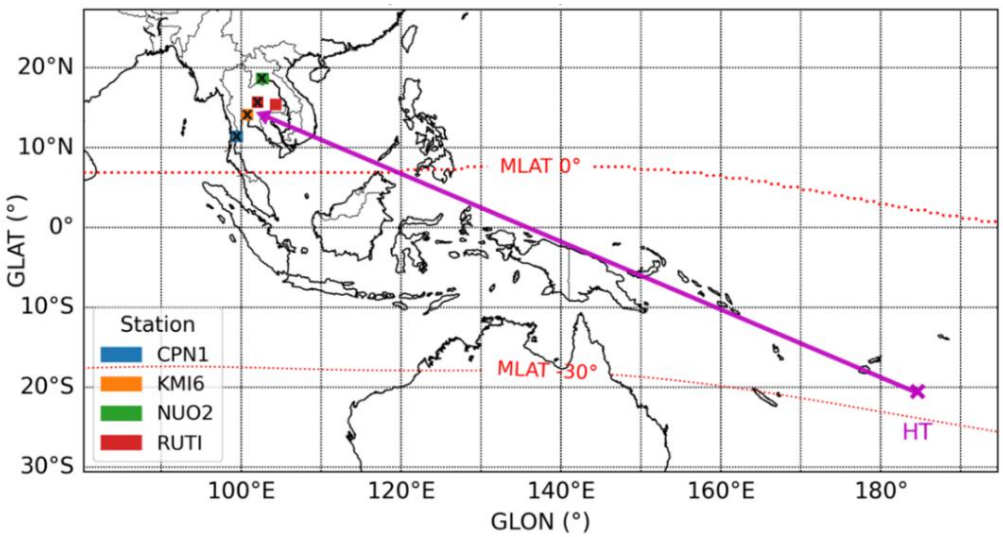


Figure 1 GNSS stations used in this study: CPN1 (blue), KMI6 (orange), and RUTI (red) in Thailand, and NUO2 (green) in Laos. These locations correspond to the stations shown in the longitude stack plots in **Figure 3**. The representative grid points nearest to each station are illustrated by black crosses within the colored squares, assuming an ionospheric pierce point (IPP) altitude of 350 km. The direction from the HT eruption (magenta cross) toward Thailand is indicated by the magenta arrow.

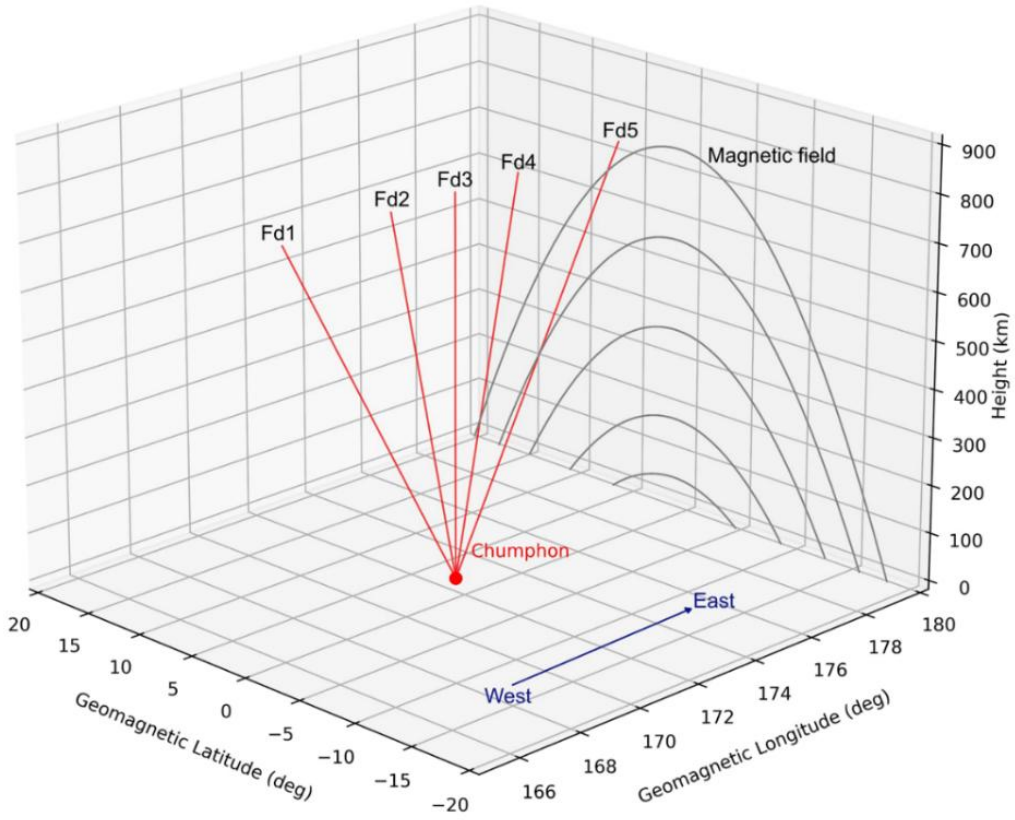


Figure 2 Map of the Chumphon station's VHF radar beams (1.33°N, 172.19°E in geomagnetic coordinates). The radar operates with 5 beams with different azimuth angles of (Fd1) −48°, (Fd2) −24°, (Fd3) 0°, (Fd4) 24°, and (Fd5) 48° from west to east, corresponding to the RATI observations shown in **Figure 8**.

Table 1 Reference ionospheric pierce point (IPP) ranges, including minimum, maximum, and median geographic latitude/longitude (GLAT/GLON) values used for VTEC, dTEC, and ROTI analysis.

Station	System	PRN	Range [min_lat°, max_ lat°], [min_ lon°, max_lon°]	Median (lat°, lon°)
CPN1	GPS	32	[−2.90, 24.33], [82.26, 116.84]	(11.42, 99.48)
KMI6	GPS	32	[−0.32, 25.30], [86.17, 115.42]	(14.16, 100.73)
NUO2	GAL	22	[13.13, 22.19], [97.57, 107.66]	(18.68, 102.70)
NUO2	GPS	29	[13.14, 22.15], [97.56, 107.67]	(18.66, 102.54)
RUTI	GPS	29	[10.19, 19.38], [97.14, 106.97]	(15.70, 102.03)
RUTI	QZS	03	[10.59, 17.44], [103.43, 106.83]	(15.42, 104.28)

Table 2 Summary of geomagnetic and ionospheric parameters during 14 - 16 January 2022.

Date	Max Kp	Min SYM-H (nT)	VTEC (TECU)		ROTI (TECU/min)		dTEC (TECU)	
			Min	Max	Min	Max	Min	Max
2022-01-14	6−	~ −101	0.00	59.32	0.00	0.88	−2.06	2.88
2022-01-15	5−	~ −78	0.00	61.62	0.00	5.55	−10.33	12.80
2022-01-16	4+	~ −53	0.00	60.93	0.00	0.77	−2.41	2.98

Results and discussion

The ionospheric disturbances associated with the volcanic eruption were analyzed using TEC-derived parameters over the region above Thailand. GNSS-derived VTEC observations were used to examine large-scale ionospheric variations through the diurnal variation of TEC. The dTEC analysis further enhanced the detection of small-scale perturbations and wave propagation structures, while ROTI measurements characterized short-term ionospheric irregularities. The geomagnetic indices indicate that the HT eruption occurred during the recovery phase of a moderate-to-strong geomagnetic storm. Therefore, geomagnetic activity is considered a potential background contributor to the observed ionospheric variability and is discussed when interpreting the timing of TEC and EPB responses. The minimum and maximum values of VTEC, ROTI, and dTEC during 14 - 16 January 2022 are summarized in Table 2 together with the corresponding geomagnetic indices. The minimum and maximum values of VTEC, ROTI, and dTEC varied substantially during 14 - 16 January 2022, as summarized in **Table 2**. To distinguish volcanic from geomagnetic influences, the maximum dTEC amplitudes and ROTI values were compared between the geomagnetic storm main phase on 14 January and the post-eruption interval on 15 January. Despite stronger geomagnetic forcing during the storm main phase (Kp = 6−, SYM-H ≈ −100 nT), the largest dTEC and ROTI disturbances were observed during the post-eruption interval, when geomagnetic activity had weakened (Kp = 5−, SYM-H ≈ −60 nT). In particular, the maximum dTEC amplitude on 15 January exceeded that on 14 January by 12.80 TECU. This comparison suggests that the enhanced ionospheric disturbances observed on 15 January were not controlled solely by geomagnetic storm intensity and are consistent with additional influences associated with the HT eruption. This quantitative comparison supports the interpretation that eruption-driven atmospheric forcing was a major contributor to the observed ionospheric disturbances during the post-eruption interval, rather than geomagnetic storm effects alone.

Main disturbance response

The main ionospheric response over Thailand was observed during the post-eruption interval on 15 January 2022. Although geomagnetic activity was at the strongest level on 14 January, VTEC variations over Thailand during the storm main phase remained

relatively weak compared with the disturbances observed after the eruption (**Figure 3**; **Table 2**). This indicates that large-scale VTEC disturbances over the study region were not strongly enhanced during the storm main phase. The 14 January observations therefore provide a useful pre-eruption reference for evaluating the stronger post-eruption ionospheric response. VHF radar observations provide an additional reference for the irregularity background. EPB1, observed on 14 January, represents a pre-eruption nighttime EPB event that developed under enhanced geomagnetic activity and is used here as a reference case (**Figure 8**). In contrast, EPB2a-2d, observed on 15 January, represent the main eruption-day EPB sequence associated with the stronger post-eruption disturbance interval.

Clear temporal correspondence was observed between enhanced dTEC structures, ROTI intensification, and VHF radar-detected EPB activity. The periods exhibiting the strongest concurrent responses are indicated as References A-C in **Figures 4**, **6** - **8**. Reference A corresponds to the initial development of strong positive dTEC enhancement and ROTI activity, whereas References B–C represent the subsequent intensification and spatial expansion of irregularity structures. Following the eruption, pronounced wave-like TEC disturbances and enhanced ionospheric irregularities were observed over Thailand. The simultaneous occurrence of enhanced dTEC structures, increased ROTI, and VHF radar signatures suggests that the large-scale TEC perturbations and irregularity development were part of the same disturbance sequence.

The first strong positive dTEC enhancement reached approximately 10 - 12 TECU. This enhancement was accompanied by clear ROTI disturbances and short-duration EPB2a activity, suggesting the onset of plasma structuring following the arrival of the eruption-related disturbances. Before this interval, only weak negative dTEC signatures were detected without corresponding ROTI enhancement, indicating that the earlier response was dominated mainly by large-scale wave propagation before significant irregularity development. During the main disturbance interval, mixed positive and negative dTEC structures were observed while irregularities expanded across nearly the entire approximately 1,000 km observation region. VHF radar measurements at CPN1 station further detected enhanced EPB2b-2c activities, including structures that rose from lower altitudes to approximately 650 - 700 km and drifted predominantly westward. This altitude range is higher than the altitude range reported for representative EPB events observed by the Chumphon VHF radar in previous studies, which typically extended to about 550 km [26,42], although more intense EPBs can reach higher altitudes [43]. The observed altitude extension is therefore consistent with enhanced irregularity development during the post-eruption disturbance interval. The simultaneous occurrence of strong dTEC disturbances, ROTI enhancement, and EPB2b-2c activities suggests possible coupling between eruption-driven atmospheric waves and low-latitude ionospheric instability processes. However, these EPBs' activities remained confined to the nighttime sector, indicating that post-sunset electrodynamic processes were still required for EPB2a-2c developments. In addition, the localized intensity and rapid upward development of some EPB structures indicate that local electrodynamic conditions may also have modulated the response. Therefore, eruption-driven disturbances may have enhanced or modulated the development of the irregularities rather than acting as the sole driver of EPB formation.

To evaluate whether the strongest TEC disturbances were temporally associated with the storm main phase or the post-eruption interval, the maximum dTEC amplitudes and ROTI values were compared between 14 and 15 January. Although geomagnetic activity was at the strongest level on 14 January, the largest dTEC and ROTI disturbances occurred on 15 January, when geomagnetic activity had weakened during the recovery phase. This comparison suggests that the enhanced ionospheric disturbances observed on 15 January were not controlled solely by geomagnetic storm intensity. Instead, the timing and magnitude of the disturbances are consistent with a major contribution from eruption-driven atmospheric forcing, although modulation by geomagnetic activity cannot be fully excluded. To quantitatively assess the eruption-related response on 15 January relative to adjacent days, dTEC measurements were compared using the Mann-Whitney U test, which is appropriate for non-Gaussian data distributions [40,41]. This statistical approach is particularly relevant for low-latitude ionospheric

observations, where substantial day-to-day variability occurs due to electrodynamic processes and plasma irregularity activity [1,20,21]. The results show statistically significant enhancements on 15 January across all stations and GNSS constellations ($p \ll 0.001$). These findings support the interpretation that the observed disturbances represent a regionally coherent eruption-associated enhancement rather than ordinary background ionospheric variability.

Propagation characteristics

Pronounced TID-like structures were observed during the initial propagation phase following the eruption. During this interval (around 08:30 UT), dTEC and VTEC exhibited well-defined positive–negative band structures, while ROTI enhancement and EPB occurrence were not yet detected. This suggests that the early response was primarily associated with large-scale wave propagation rather than fully developed plasma irregularities. The progression of the propagation pattern is indicated by transitions 1′ - 6′ in **Figures 4** and **5**.

The propagation velocity estimated from the early disturbance features was approximately 427 ± 19 m/s. This velocity, corresponding to Transitions 1′ - 2′, is comparable to fast atmospheric wave components and secondary gravity waves reported in previous Hunga Tonga studies. The disturbances propagated generally westward across the observation region, consistent with the arrival of eruption-related atmospheric–ionospheric wave disturbances over Thailand. A later disturbance sequence propagated with an estimated velocity of approximately 312 ± 13 m/s. This velocity, corresponding to Transitions 3’ - 4’, is consistent with typical propagation velocities reported for Lamb-wave-related TIDs and acoustic–gravity wave disturbances. The occurrence of multiple apparent propagation speeds suggests that more than one atmospheric wave component contributed to the observed ionospheric response. The faster component ($V_{1'-2'}$) likely represents an early-arriving wave structure, while the later $V_{3'-4'}$ disturbance is more consistent with Lamb-wave-related propagation.

During the main propagation phase, approximately 8 h after the eruption, the disturbance sequence became more complex. Stronger dTEC enhancements were observed together with increased ROTI values, indicating that large-scale wave perturbations were accompanied by rapid TEC fluctuations and irregularity-related plasma structuring. The development from coherent TID-like propagation to enhanced ROTI and EPB2a-2c activities suggests a progressive evolution from large-scale wave arrival to plasma instability growth. The dTEC structures became less coherent as the disturbances evolved farther along the propagation path, corresponding to Transitions 5′ - 6′. Regions closer to the eruption direction showed clearer double-peaked enhancement patterns, whereas more distant regions exhibited weaker or mixed positive–negative dTEC variations. This behavior suggests that the propagating disturbances gradually lost coherence and amplitude with increasing distance, likely due to dissipation, dispersion, and interaction with background ionospheric structures or multiple wave components. Overall, the propagation features indicate strong and spatially coherent ionospheric forcing during the early and main disturbance phases, followed by weakening of wave structures at greater distances and later times.

Post-event behavior

After the main disturbance interval, the ionosphere over Thailand showed evidence of continued variability and partial recovery. Around the pre-midnight period, EPB2d was observed in the VHF radar data. Although corresponding ROTI measurements were unavailable during this interval, weak dTEC variations were detected, suggesting possible ionospheric irregularity activity during this period. On 16 January, daytime VTEC and dTEC observations showed reduced TEC conditions relative to the pre-storm interval. This behavior is consistent with possible recovery processes involving plasma recombination, modified electrodynamics, and disturbed neutral atmosphere conditions following earlier ionospheric perturbations. The post-event TEC conditions may reflect combined influences from geomagnetic storm recovery, residual eruption-related disturbances, and ordinary low-latitude ionospheric variability. Previous studies have reported that eruption-induced electrodynamic disturbances and large-scale atmospheric waves associated with the Hunga Tonga eruption could persist for extended periods and continue to modulate ionospheric plasma distributions on subsequent days. However,

distinguishing the relative contributions of geomagnetic storm recovery and remaining eruption-related effects requires additional observational and modeling studies.

During the post-sunset period on 16 January, weak EPB activity (EPB3) was detected together with weak dTEC variations (**Figures 4** and **8**). Because both geomagnetic disturbances and eruption-driven atmospheric waves can modulate EPB occurrence and plasma instability growth, it remains difficult to determine whether EPB3 was primarily associated with storm-time electrodynamics, residual eruption-related disturbances, or ordinary post-sunset EPB generation processes. Nevertheless, the relatively weak dTEC variations observed during this interval suggest that ionospheric forcing was substantially weaker than during the main disturbance phase on 15 January. Overall, the observed ionospheric signatures suggest a progressive sequence from large-scale TID propagation to enhanced TEC fluctuations, increased ROTI, and subsequent EPB development. Although geomagnetic activity likely contributed to background ionospheric variability and electrodynamic conditions, the timing, propagation characteristics, and spatial coherence of the 15 January response are more consistent with a major contribution from eruption-driven atmospheric waves superimposed on geomagnetic background conditions.

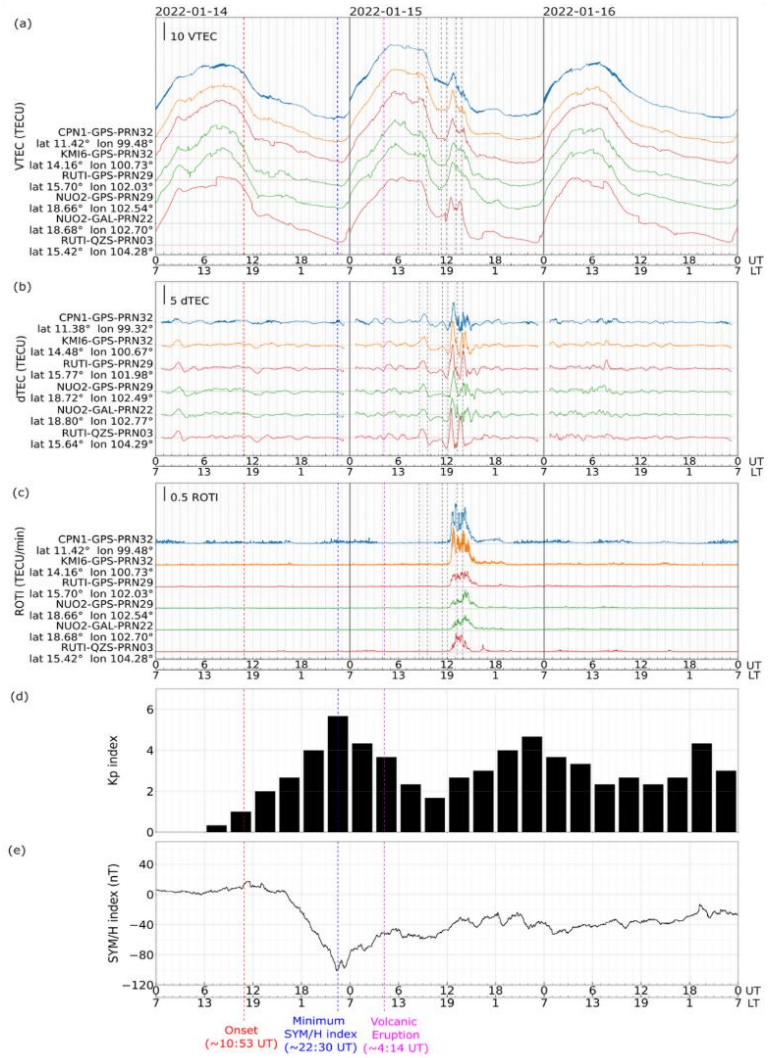


Figure 3 Longitude-time stack plots of (a) VTEC, (b) dTEC, and (c) ROTI derived from 6 representative positions from 4 GNSS receiver stations (CPN1, KMI6, RUTI and NUO2), indicated by the colored squares in **Figure 1**. Panels (d) and (e) show the Kp and SYM-H indices, respectively, during the geomagnetic storm and the HT eruption. The onset of the geomagnetic storm at ~10:53 UT on 14 January is marked by a red dashed line, while the beginning of the recovery phase at the minimum SYM-H value (~22:30 UT on 14 January) is indicated by a blue dashed line. The volcanic eruption at ~04:14 UT on 15 January is denoted by the magenta dashed line.

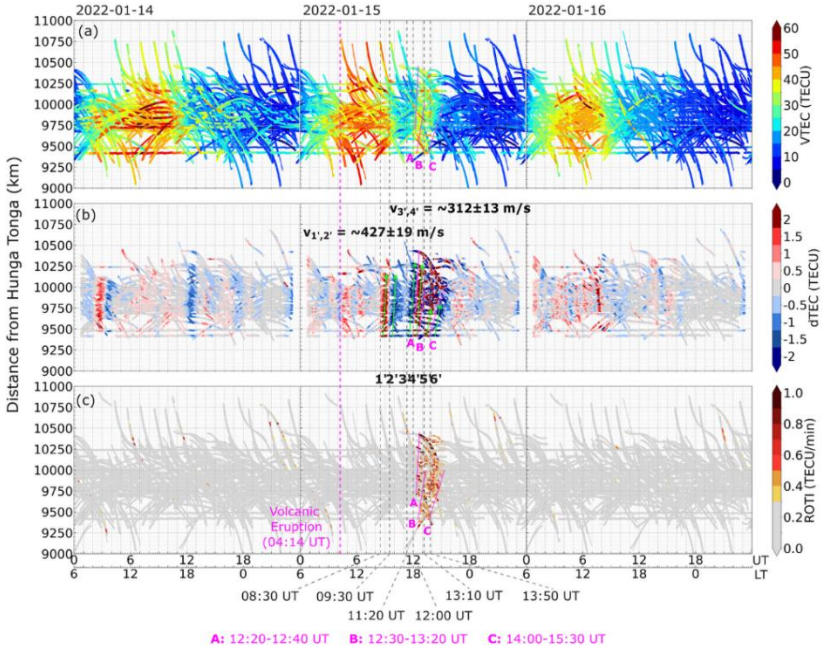


Figure 4 Distance-time plots of (a) VTEC, (b) dTEC, and (c) ROTI derived from the GNSS observations during 14 - 16 January 2022. The magenta dashed line indicates the onset of the HT eruption at 04:14 UT on 15 January 2022. Grey dashed lines denote prominent wave-like disturbances propagating along the great-circle path from the HT eruption. The main ionospheric disturbances in all parameters appear approximately 8 h after the eruption.

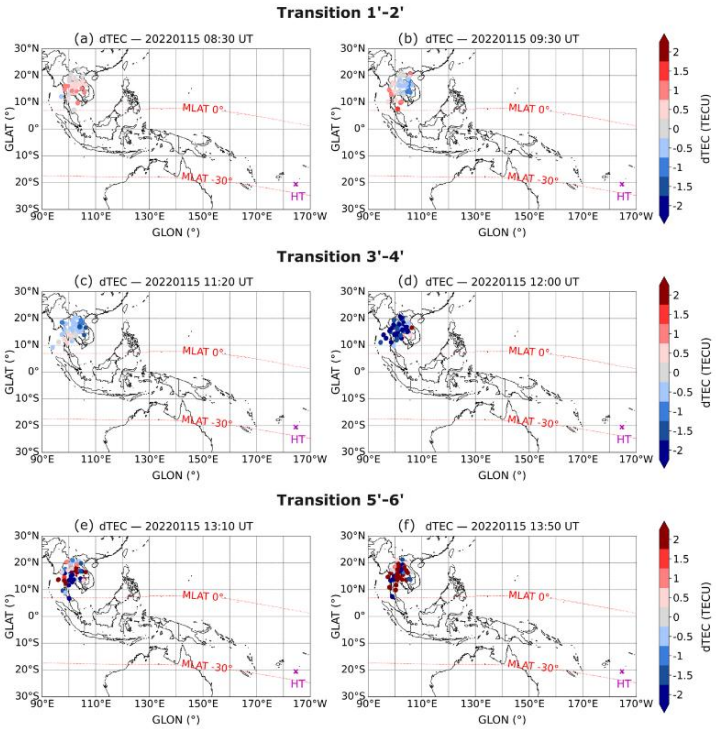


Figure 5 Time-stamped dTEC map plots showing the spatial variations and propagation directions during 3 transition intervals associated with significant dTEC changes. Transition 1′ - 2′ correspond to the onset of (a) positive dTEC (red) at 08:30 UT and (b) negative dTEC (blue) at 09:30 UT. Transition 3′ - 4′ correspond to (c) positive dTEC (red) at 11:20 UT and (d) negative dTEC (blue) at 12:00 UT, while Transition 5′ - 6′ corresponds to (e) positive dTEC (red) at 13:10 UT and (f) negative dTEC (blue) at 13:50 UT. The propagation directions are indicated by the 3 paired green arrows shown in **Figure 4**.

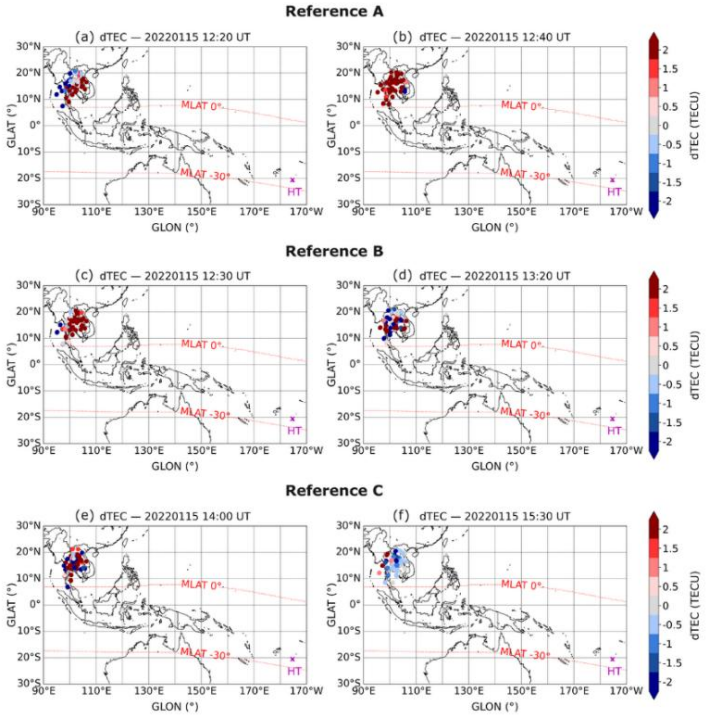


Figure 6 Time-stamped dTEC map plots showing the spatial variations and propagation directions from the onset to the end of References A - C, marked by the 3 solid magenta lines in **Figure 4(b)**. These dTEC features during these intervals occur simultaneously with the corresponding VTEC and ROTI signatures shown in **Figures 4(a)** and **4(c)**, respectively. Reference A is shown at (a) 12:20 UT and (b) 12:40 UT, Reference B at (c) 12:30 UT and (d) 13:20 UT, and Reference C at (e) 14:00 UT and (f) 15:30 UT.

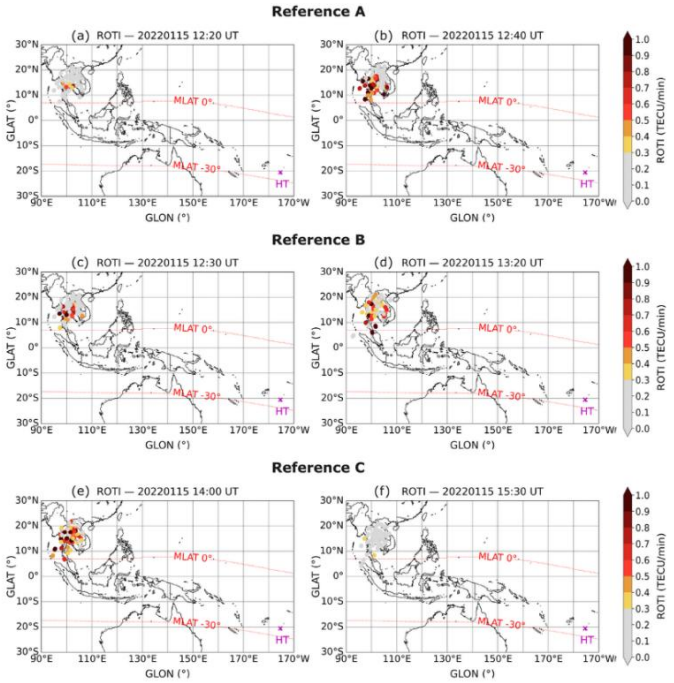


Figure 7 Time-stamped ROTI map plots showing the spatial variations and propagation directions from the onset to the end of References A - C, marked by the 3 solid magenta lines in **Figure 4(c)**. The ROTI features during these intervals occur simultaneously with the corresponding VTEC and dTEC signatures shown in **Figures 4(a)** and **4(b)**, respectively. Reference A is shown at (a) 12:20 UT and (b) 12:40 UT, Reference B at (c) 12:30 UT and (d) 13:20 UT, and Reference C at (e) 14:00 UT and (f) 15:30 UT.

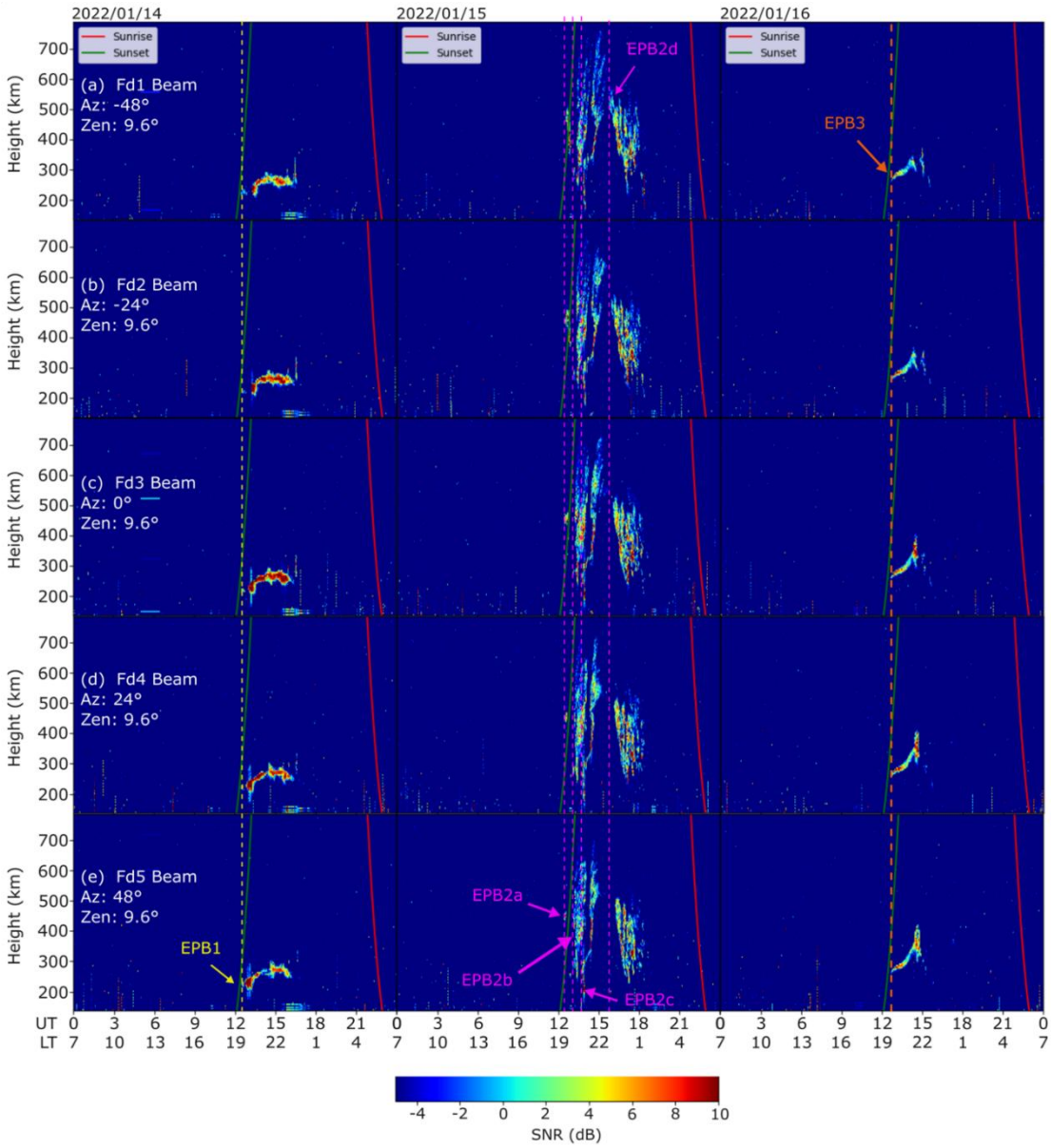


Figure 8 Range-Altitude-Time Intensity (RATI) observations from 14 - 16 January 2022 for 5 radar beams with a zenith angle of 9.6° and azimuth angles of (a) −48°, (b) −24°, (c) 0°, (d) 24°, and (e) 48° from west to east. The corresponding 3D beam geometry is illustrated in **Figure 2**. The solid red and green lines indicate the time of sunrise and sunset, respectively. The RATI observations reveal EPB activity during the interval surrounding the HT eruption under concurrent geomagnetic storm conditions. The onset times of the EPBs are indicated by dashed lines.

The observed ionospheric signatures suggest a close association between large-scale wave propagation and plasma instability development. Initial TID arrival was followed by enhanced plasma structuring, and subsequent EPB development. This temporal sequence indicates a progressive evolution of atmospheric-ionospheric disturbances rather than isolated events.

The early-phase TID activity may have provided seed perturbations favorable for plasma instability growth in the low-latitude ionosphere [3,7,8]. The subsequent increase in ROTI and the emergence of large-scale EPBs suggest enhanced nonlinear development and vertical extension of plasma depletion structures associated with RTI growth [7,18]. Similar transitions from coherent wave propagation to enhanced plasma irregularities have been reported in previous studies of the Tonga eruption and interpreted as evidence of coupling between eruption-driven atmospheric waves and low-latitude ionospheric electrodynamics [7,8,13,30].

Although geomagnetic activity likely contributed to the background ionospheric variability and electrodynamic conditions, the observed temporal evolution, propagation characteristics, and spatial coherence are consistent with a major contribution from eruption-driven atmospheric waves during the main disturbance interval. The timing and morphology of the ionospheric response therefore suggest strong influence from eruption-driven disturbances superimposed on geomagnetic background conditions.

Conclusions

This study presents GNSS-TEC and VHF radar observations of ionospheric variability over Thailand associated with the 15 January 2022 Hunga Tonga-Hunga Ha'apai volcanic eruption. Disturbance signatures were detected approximately 8 h after the eruption, and exhibited clear wave-like dTEC structures with amplitudes of approximately 10 - 12 TECU, consistent with TIDs. The associated disturbances propagated toward Thailand with an estimated horizontal propagation speed of approximately 312 ± 13 m/s, consistent with acoustic-gravity and Lamb-wave propagation speeds [3,13,14]. ROTI enhancements were observed concurrently with the main dTEC wave features, indicating the presence of strong ionospheric irregularities during the disturbance interval. VHF radar measurements from the CPN1 station further revealed enhanced EPB activity on the eruption day. The EPBs exhibited substantial vertical development, with plasma irregularities extending to approximately 650 - 700 km altitude and irregularity regions extending over ∼1,000 km horizontally, indicating large-scale irregularity development during the post-eruption disturbance interval.

The temporal correspondence between TID signatures, ROTI enhancement, and EPB development is consistent with a dynamically coupled response, in which large-scale wave disturbances may have influenced the growth and morphology of plasma irregularities. Although the eruption occurred under concurrent geomagnetic storm recovery conditions, the most pronounced disturbances over Thailand were observed during the post-eruption interval, and the observed disturbance magnitudes were larger than those during the preceding geomagnetically active interval. Smaller TEC perturbations on the following day imply that additional background processes remained active and may also have contributed to regional variability. Overall, these observations provide a regional reference for ionospheric responses over Thailand during the Hunga Tonga eruption. The timing, propagation characteristics, and spatial coherence of the main disturbances are consistent with a major contribution from eruption-driven atmospheric waves, although modulation by geomagnetic activity cannot be fully excluded. The results also provide useful context for assessing potential impacts on GNSS-based navigation and radio communication systems in low-latitude Southeast Asia.

Research limitations

This study focuses on the Hunga Tonga volcanic eruption, which represents an exceptionally strong and rare event. As such, the statistical generality of the results is limited, and additional events are required to further validate the findings. The analysis is based on observations over Thailand, where high-resolution temporal and spatial variations of ionospheric irregularities can be examined. However, the propagation characteristics of TIDs would be more comprehensively assessed through coordinated observations across neighboring regions. Such regional comparisons would help to better constrain the horizontal propagation and evolution of the disturbances.

In addition, this work is primarily based on ground-based observations. Investigation of the global ionospheric response would benefit from the inclusion of satellite-based measurements or numerical modeling, which can provide a broader spatial context and support interpretation of large-scale coupling processes. Future work may also include the development of an ionospheric model over Thailand using the observational dataset presented here. This would help improve understanding of ionospheric response mechanisms in the low-latitude region, where observations remain limited, particularly in Southeast Asia.

Acknowledgements

Special thanks to the Development and Promotion of Science and Technology Talents Project (DPST) scholarship, Royal Government of Thailand. We

acknowledge the Chalawan High Performance Computing (HPC) Cluster from the National Astronomical Research Institute of Thailand (NARIT). This research project is supported by the NSRF via the Program Management Unit for the Human Resources and Institutional Development, Research and Innovation (Grant no. B41G690022). The KMI6 and CPN1 GNSS data are provided by the Thai GNSS and Space Weather Information Data Center hosted at King Mongkut's Institute of Technology Ladkrabang (KMITL), Thailand (http://iono-gnss.kmitl.ac.th). The VHF data are contributed from the Southeast Asia Low-latitude IOnosphere Network (SEALION) under the National Institute of Information and Communications Technology (NICT) service (https://aer-nc-web.nict.go.jp/sealion/index.html). This research was partially supported by Chiang Mai University. Larry J. Paxton acknowledges support from NASA contract 80NSSC24K0387. This project is funded by National Research Council of Thailand (NRCT) and King Mongkut's Institute of Technology Ladkrabang (N42A690146).

Declaration of Generative AI in Scientific Writing

The authors acknowledge the use of generative AI tools in the preparation of this manuscript. Specifically, ChatGPT by OpenAI was used for language editing and grammar correction, while Google Flow was used to support the layout and design concept of the graphical abstract. The authors take full responsibility for the content and conclusions of this work.

CRediT Author Statement

Paparin Jamlongkul: Conceptualization; Data curation; Methodology; Investigation; Visualization; Writing - Original draft preparation. **Suwicha Wannawichian**: Conceptualization; Methodology; Data curation; Visualization; Investigation; Writing - Original draft preparation. **Larry J. Paxton**: Conceptualization; Methodology; Writing - Review & Editing. **Clayton E. Cantrall**: Conceptualization; Writing - Review & Editing **Pornchai Supnithi**: Supervision. **Jirapoom Budtho**: Data curation. **Napat Tongkasem**: Data curation; Software; Writing - Review & Editing. **Thananphat Thanakulketsarat**: Data curation. **Phimmasone Thammavongsy**: Data curation. **Michi Nishioka**: Data curation.

References

[1] Y Liu, L Fu, J Wang and C Zhang. Studying ionosphere responses to a geomagnetic storm in June 2015 with multi-constellation observations. *Remote Sensing* 2018; **10(5)**, 666.

[2] S Saito. Ionospheric disturbances observed over Japan following the eruption of Hunga Tonga-Hunga Ha'apai on 15 January 2022. *Earth Planets Space* 2022; **74(1)**, 57.

[3] A Shinbori, Y Otsuka, T Sori, N Michi, S Perwitasari, T Takuo, N Nozomu, K Atsushi, T Fuminori, M Shoya, K Yoshiya, M Ayako, N Satoko, M Yoshizumi and S Iku. New aspects of the upper atmospheric disturbances caused by the explosive eruption of the 2022 Hunga Tonga-Hunga Ha'apai volcano. *Earth Planets Space* 2023; **75(1)**, 175.

[4] R Pradipta, B A Carter, JL Currie, S Choy, P Wilkinson, P Maher and R Marshall. On the propagation of traveling ionospheric disturbances from the Hunga Tonga-Hunga Ha'apai volcano eruption and their possible connection with tsunami waves. *Geophysical Research Letters* 2023; **50(6)**, e2022GL101925.

[5] V Rakesh, S Haridas, C Sivan, MG Manoj, S Abhilash, B Paul, K Unnikrishnan, K Mohanakumar and RS Chandran. Impact of the Hunga Tonga-Hunga Ha'apai volcanic eruption on the changes observed over the Indian near-equatorial ionosphere. *Advances in Space Research* 2022; **70(8)**, 2480-2493.

[6] X Li, F Ding, X Yue, T Mao, B Xiong and Q Song. Multiwave structure of traveling ionospheric disturbances excited by the Tonga volcanic eruptions observed by a dense GNSS network in China. *Space Weather* 2023; **1(2)**, e2022SW003210.

[7] W Sun, AK Kuriakose, G Li, Y Li, X Zhao, L Hu, S Yang, H Xie, Y Li, B Ning and L Liu. Unseasonal super ionospheric plasma bubble and scintillations seeded by the 2022 Tonga volcano eruption related perturbations. *Journal of Space Weather and Space Climate* 2022; **12(25)**, 25.

[8] J Hong, H Kil, W K Lee, YS Kwak, BK Choi and LJ Paxton. Detection of different properties of ionospheric perturbations in the vicinity of the Korean Peninsula after the Hunga-Tonga volcanic

eruption on 15 January 2022. *Geophysical Research Letters* 2022; **49(14)**, e2022GL099163.

[9] E Astafyeva, B Maletckii, TD Mikesell, E Munaibari, M Ravanelli, P Coisson, F Manta and L Rolland. The 15 January 2022 Hunga Tonga eruption history as inferred from ionospheric observations. *Geophysical Research Letters* 2022; **49(10)**, e2022GL098827.

[10] E Aa, SR Zhang, W Wang, PJ Erickson, L Qian, R Eastes, BJ Harding, TJ Immel, DK Karan, RE Daniell, AJ Coster, LP Goncharenko, J Vierinen and A Spicher. Pronounced suppression and X-pattern merging of equatorial ionization anomalies after the 2022 Tonga volcano eruption. *Journal of Geophysical Research: Space Physics* 2022; **127(6)**, e2022JA030527.

[11] IN Muafiry, I Meilano, K Heki, DD Wijaya and KA Nugraha. Ionospheric disturbances after the 2022 Hunga Tonga-Hunga Ha'apai eruption above Indonesia from GNSS-TEC observations. *Atmosphere* 2022; **13(10)**, 1615.

[12] K Tarumi and K Yoshizawa. Eruption sequence of the 2022 Hunga Tonga-Hunga Ha'apai explosion from back-projection of teleseismic P waves. *Earth and Planetary Science Letters* 2023; **602**, 117966.

[13] SL Vadas, E Becker, C Figueiredo, K Bossert, BJ Harding and LC Gasque. Primary and secondary gravity waves and large-scale wind changes generated by the Tonga volcanic eruption on 15 January 2022: Modeling and comparison with ICON-MIGHTI winds. *Journal of Geophysical Research: Space Physics* 2023; **128(2)**, e2022JA031138.

[14] K Heki. Ionospheric signatures of repeated passages of atmospheric waves by the 2022 Jan. 15 Hunga Tonga-Hunga Ha'apai eruption detected by QZSS-TEC observations in Japan. *Earth Planets Space* 2022; **74(12)**, 112.

[15] K Shults, E Astafyeva and S Adourian. Ionospheric detection and localization of volcano eruptions on the example of the April 2015 Calbuco events. *Journal of Geophysical Research: Space Physics* 2016; **121(10)**, 10303-10315.

[16] LFR Vital, J Xu, Y Otsuka, TT Ayorinde, H Takahashi, D Barros, CS Carmo, CAOB Figueiredo, CM Wrasse, LM Lima, I Paulino, C Wang, H Li and L Zhengkuan. On the fresh development of midnight plasma bubbles over South America. *Earth Planets and Space* 2025; **77(1)**, 131.

[17] Y Otsuka. *Ionosphere dynamics and applications*. John Wiley & Sons, New Jersey, 2021, p. 421-437.

[18] MJ Keskinen, SL Ossakow and BG Fejer. Three-dimensional nonlinear evolution of equatorial ionospheric spread-F bubbles. *Geophysical Research Letters* 2003; **30(16)**, 1855

[19] T Sori, Y Otsuka, A Shinbori, M Nishioka and S Perwitasari. Geomagnetic conjugacy of plasma bubbles extending to mid-latitudes during a geomagnetic storm on March 1, 2013. *Earth Planets Space* 2022; **74(1)**, 120.

[20] Y Otsuka. Review of the generation mechanisms of post-midnight irregularities in the equatorial and low-latitude ionosphere. *Progress in Earth and Planetary Science* 2018; **5(1)**, 57.

[21] MM Miller, JJ Makela and MC Kelley. Seeding of equatorial plasma depletions by polarization electric fields from middle latitudes: Experimental evidence. *Geophysical Research Letters* 2009; **36(18)**, L18105.

[22] H Takahashi, CM Wrasse, CAOB Figueiredo, D Barros, MA Abdu, Y Otsuka and K Shiokawa. Equatorial plasma bubble seeding by MSTIDs in the ionosphere. *Progress in Earth and Planetary Science* 2018; **5(1)**, 32.

[23] X Pi, AJ Mannucci, UJ Lindqwister and CM Ho. Monitoring of global ionospheric irregularities using the worldwide GPS network. *Geophysical Research Letters* 1997; **24(18)**, 2283-2286.

[24] MA Kelly, JM Comberiate, ES Miller and LJ Paxton. Progress toward forecasting of space weather effects on UHF SATCOM after Operation Anaconda. *Space Weather* 2014; **12(10)**, 601-611.

[25] H Nakata, I Nagashima, K Sakata, Y Otsuka, Y Akaike, T Takano, S Shimakura, K Shiokawa and T Ogawa. Observations of equatorial plasma bubbles using broadcast VHF radio waves. *Geophysical Research Letters* 2005; **32(17)**, L17110.

[26] T Thanakulketsarat, P Supnithi, LMM Myint, K Hozumi and M Nishioka. Classification of the equatorial plasma bubbles using convolutional

neural network and support vector machine techniques. *Earth Planets Space* 2023; **75(1)**, 161.

[27] Y Otsuka, T Ogawa and Effendy. VHF radar observations of nighttime F-region field-aligned irregularities over Kototabang, Indonesia. *Earth, Planets Space* 2009; **61(4)**, 431-437.

[28] S Fukao, MC Kelley, T Shirakawa, T Takami, M Yamamoto, T Tsuda and S Kato. Turbulent upwelling of the mid-latitude ionosphere, 1. observational results by the MU radar. *Journal of Geophysical Research* 1991; **96(A3)**, 3725-3746.

[29] T Charoenkalunyuta, C Satirapod, HK Lee and YS Choi. Performance of networkbased RTK GPS in low-latitude region: A case study in Thailand. *Engineering Journal* 2012; **16(5)**, 95-104.

[30] E Aa, SR Zhang, PJ Erickson, J Vierinen, AJ Coster, LP Goncharenko, A Spicher and W Rideout. Significant ionospheric hole and equatorial plasma bubbles after the 2022 Tonga volcano eruption. *Space Weather* 2022; **20(7)**, e2022SW003101.

[31] A Bumrungkit, P Supnithi and S Saito. Statistical analysis of separation distance between equatorial plasma bubbles near Suvarnabhumi International Airport, Thailand. *Journal of Geophysical Research: Space Physics* 2018; **123(9)**, 7858-7870.

[32] N Ya'Acob, M Abdullah and M Ismail. *GPS Total Electron Content (TEC) prediction at ionosphere layer over the equatorial region.* In: CJ Bouras (Ed.). Trends in telecommunications technologies. IntechOpen, Rijeka, Croatia, 2010.

[33] G Blewitt. Carrier phase ambiguity resolution for the global positioning system applied to geodetic baselines up to 2000 km. *Journal of Geophysical Research* 1989; **94(B8)**, 10187-10203.

[34] G Ma and T Maruyama. Derivation of TEC and estimation of instrumental biases from GEONET in Japan. *Annales Geophysicae* 2023; **21(10)**, 2083-2093.

[35] L Kersley, D Malan, SE Pryse, LR Cander, RA Bamford, A Belehaki, R Leitinger, SM Radicella, CN Mitchell and PSJ Spencer. Total electron content - a key parameter in propagation: measurement and use in ionospheric imaging. *Annales Geophysicae* 2004; **47(2/3)**, 1067-1091.

[36] RK Vankadara, P Jamjareegulgarn, GK Seemala, MdIH Siddiqui and SK Panda. Trailing equatorial plasma bubble occurrences at a low-latitude location through multi-GNSS Slant TEC depletions during the strong geomagnetic storms in the ascending phase of the 25th solar cycle. *Remote Sensing* 2023; **15(20)**, 4944.

[37] I Cherniak, I Zakharenkova and A Krankowski. IGS ROTI maps: Current status and its extension towards equatorial region and southern hemisphere. *Sensors* 2022; **22(10)**, 3748.

[38] NASA/GSFC's space physics data facility's OMNI webservice, Available at: https://omniweb.gsfc.nasa.gov, accessed August 2023.

[39] World Data Center for Geomagnetism, Available at: https://wdc.kugi.kyoto-u.ac.jp, accessed February 2026.

[40] HB Mann and DR Whitney. On a test of whether one of two random variables is stochastically larger than the other. *The Annals of Mathematical Statistics* 1947; **18(1)**, 50-60.

[41] PF Michael and AP Michael. Wilcoxon-Mann-Whitney or t-test? On assumptions for hypothesis tests and multiple interpretations of decision rules. *Statistics Surveys* 2010; **4**, 1-39.

[42] N Tongkasem, P Supnithi, M Nishioka, S Perwitasari, S Saito, J Klenzing and LMM Myint. Spatio-temporal characteristics of ionospheric irregularities in low latitude regions during the peak of solar cycle 25. *Advances in Space Research* 2025; **76(1)**, 254-268.

[43] T Yokoyama, H Shinagawa and H Jin. Nonlinear growth, bifurcation and pinching of equatorial plasma bubble simulated by three-dimensional high-resolution bubble model. *Journal of Geophysical Research: Space Physics* 2014; **119(12)**, 10474-10482.